Templated assembly of micropatterned Au-Ni nanoparticles on laser interference-structured surfaces by thermal dewetting

Lu Wang, Litong Dong, Li Li, Ran Ding, Jinyun Liu, Wenxiao Zhang, Ying Wang, Zhankun Weng, Xudong Guo, Zuobin Wang

Abstract

In this paper, we introduce a method for the assembly of micropatterned bimetallic nanoparticles (NPs) withcontrollable patterns and particle sizes on laser interference-structured substrates. The microstructures of interference patterning in conjunction with the nanostructures fabricated by the direct laser interference ablation (DLIA) were used as the templates for the assembly of patterned NPs in thermal dewetting processes. The location and particle size of micropatterned Au-Ni NPs formed were well-controlled by the nanostructures on the substrate surface. The magnetic domain pattern of as-annealed Au-Ni NPs is consistent with the topography of the silicon templates. The DLIA method provides a one-step new way for the large-area and high throughput fabrication of patterned NPs with the templated dewetting method. It can be easily extended to many metal combinations and has wide applications such as magnetic recording, plasmon-enhancement and other functional nanostructured elements and devices

1. Introduction

Micro and nano-patterned nanoparticles (NPs) are attracting more recognition recently due to their widespread applications such as plasmon resonance devices [1,2], surface-enhanced Raman scattering (SERS) [3,4], photocatalysts [5,6], catalysts for the growth of carbon nanotubes and nanowires [7,8], high-density data storage devices [9,10] and sensors [11,12]. Furthermore, the bimetallic NPs, incorporating heterometals into noble metals, can tune chemical and physical properties of NPs and show an enhancement in performance [13]. Especially, the patterned Au-Ni NP arrays exhibit magnified ferromagnetic behavior, due to the interaction between the Ni particles and the Au surface layer [14,15]. This can be used to obtain high efficient SERS substrates and patterned magnetic recording devices. Direct assembly of NPs on the lithographically-defined features is the common method for large-scale and fast production of ordered NPs [16,17]. The strategies include the assembly of colloids into organized patterns [18], controllable chemical syntheses on liquid-substrate interface [19] and templated dewetting. Among the methods, template dewetting has been much reviewed and regarded as a most straightforward method to induce self-assembly of ordered metal NPs [20]. Conventional templated dewetting requires a multistep lithographic process, such as interference lithography (IL) [21,22], nanoimprint lithography (NIL) [23,24] or nanosphere lithography (NSL) [25]. It is able to control the location and size of individual NPs by the breakup and retraction of the films, but it can hardly control the spacing between NPs or their densities on the nanoscale, limited by the feature size of lithographically-defined structures. Tuning the Rayleigh instability during the self-assembly process is another emerging strategy for ordered NP arrays. NP arrays with a controllable size and spacing were obtained by dewetting of nanoscale patterned metal thin film strips [26,27]. This method has excellent control over the size and spacing between the NPs but is restricted by low throughput and high cost. The appropriate templates that both have the large-area patterning capability and the dewettability function for the precise control of NPs remains a fundamental challenge.

In this work, we used the periodical dual-scale micro/nano structures on the substrate surfaces fabricated by the direct laser interference ablation (DLIA) method as the templates to regulate the assembly of NPs. The DLIA method offers a fast and accurate alternative to fabricate the templates without chemical, mask and pattern transfer processes [28–30]. The fabricated

dual-scale surface structures were suitable templates for the precise control of the pattern and size of NPs as functional dewetting [31]. Hexagonally patterned Au–Ni NP arrays were obtained by thermal dewetting of Au-Ni bilayer films. The mechanism of fabricating dual-scale surface structures by the DLIA method was analyzed. The effects of laser interference fluences on the micro/nano structures and the effects of dual-scale structures on driving the dewetting process were quantified and discussed subsequently. Smaller and more uniformly distributed NPs with narrow spacings were obtained in the case of increasing roughness due to the modified Rayleigh instability. In addition, the magnetic domain pattern of as-annealed Au-Ni NP arrays is in agreement with the topographical pattern of the NPs as well as the silicon templates. The generated micropatterned NPs can be integrated into functional structures to produce nanodevices by transfer printing. This method provides a new way for the large-area and high throughput fabrication of patterned nanoparticle arrays with the controllable pattern and size.

2. Material and methods

2.1. Experiment

2.1.1. Laser interference ablation

The DLIA method was carried out by irradiating the silicon surfaces using a nanosecond Q-switched Nd:YAG laser (Innolas) with the wavelength of 1064nm, frequency of 10Hz and pulse duration of 7ns in a three-beam interference system. The P-type (100) oriented polished silicon wafers were used for the experiments and they were carried out under ambient condition. The schematic of the three-beam interference ablation system setup is shown in Fig. 1(a). In the experiments, the three incident beams followed a symmetrical configuration with the azimuthal angles of $\varphi1=0°$, $\varphi2=120°$ and $\varphi3=240°$ and the same incident angle of 4.1°. In the TE-TE-TE polarization mode, the laser intensity distribution (LID) of the laser interference pattern is shown in the inset of Fig. 1(a). The period of two-beam interference pattern is $d=\lambda/2\sin(\theta)$, thus the side length of one hexagonal cell in Fig. 1(c) is approximately 5μm based on the theoretical calculation of three-beam interference. The interference laser energy was measured with an energy meter (COHERENT LabMax-top) in front of the sample surface. According to the irradiated area, the laser energy was transformed to the laser fluence. The side length of one hexagonal cell in the blue square of Fig. 1(b) is approximately 5μm based on the theoretical calculation of three-beam interference. In the experiments, the influence of different laser fluences ranging from 300 to 600mJ/cm2 and 30 pulses were used to determine the optimum does for the ablation.

2.1.2. Bilayer deposition

The Au-Ni films were deposited onto the as-ablated Si substrates using a Turbo sputter carbon coater, Q150T (Quorum Technologies). The Ar flow was used during the deposition at the pressure of 10−mbar in the chamber and the target-surface distance of 40mm. The bilayer thickness was 10nm each in order to obtain the desired NPs upon annealing. The deposition accuracy was determined to be about 5% of film thickness. Au was chosen on the top in order to avoid the oxidation when exposed to air and the synthesis of gold-silica composite [32]. Also, an Au-Ni bilayer of 10nm each was deposited on a bare Si surface with the same condition for comparison.

2.1.3. Thermal processing

Rapid thermal annealing (KJ GROUP OTF-1200X-4-RTP) was used to induce the dewetting of Au/Ni bilayer thin films on the as-deposited substrates, and it was carried out at 950°C for 300s with a subsequent cooling process in furnace. There is a wide miscibility gap and a homogeneous region at high temperatures in the equilibrium Au-Ni phase diagram [33–35]. Thus, rapid thermal annealing with the temperatures from 800°C to 950°C, and the time from 60s to 500s were used for the experiments. Shorter time or lower temperature would lead to

uncompleted dewetting and flat particles, while longer time would obtain the synthesis of gold-silica composites. Thus, the temperature of 950°C and time of 300s were chosen for the experiments. Vacuum annealing was used to avoid oxidation and contamination during the annealing treatment of samples. A heating rate of 50°Cs−1 was used and the fast cooling was performed by simply switching off the heating. Fig. 1(b) shows the as-annealed Au-Ni NP arrays. A low magnification SEM image of NP arrays showing the ordering of hexagonal cells was also provided (Supporting Information S1).

2.2. Characterization

Atomic force microscopy (AFM) analyses were performed by a JPK microscope (NanoWizard®3) with ultra-sharpened Si tips (SNL-W from APPNANO, with the anisotropic geometry, radius of curvature~2nm and tip thickness~0.6μm) in the contact mode for the as-ablated silicon topography imaging. The magnetic force microscope (MFM) system was used for the imaging of the magnetic properties of the dewetted Au-Ni NPs in the air condition. The spring constant of the magnetic probe was 3N/m and the resonant frequency was 75kHz (MagneticMulti75-G, Budget Sensors). All the AFM and MFM images were analyzed using the JPK Data Processing software (Version spm-6.0.65). A scanning electron microscope (SEM) was used to examine the morphological characteristics of the silicon templates and the grain distributions of the as-annealed NPs. All samples were imaged by a high-resolution SEM (FEI QUANT-250 FEG, at the 5kV accelerated voltage). The SEM was equipped with an energy-dispersive x-ray spectrometer (EDS, Oxford Instruments) detection system, which was performed in the map scan mode, line scan mode and point scan mode, respectively, at 15kV to detect the element distributions of Au M and Ni L lines. Transmission electron microscopy (TEM) and high resolution transmission electron microscopy (HRTEM) sample observations were carried out with a JEM-2100F transmission electron microscope, operating at 200keV. Magnetic measurements were performed using a superconducting quantum interference device (SQUID) magnetometer (Quantum Design-MPMS-XL7).

The distributions of chemical compositions and sizes of particles are shown in Fig. 2. Fig. 2(a) shows the SEM image and EDS mapping image of the dewetted Au-Ni bi-metal particles within one hexagonal cell on the silicon after annealing at 950°C for 300s, and the overlap of the Au (green), Si (red) and Ni (pink) EDS maps. The elemental map clearly demonstrated that the Au and Ni were uniformly distributed throughout the template silicon. The EDS maps of the dewetted particles indicate a homogeneous Au-Ni solid solution formed without the Ni-rich or Au-rich distribution, and the overall particles are spherical. Higher magnification EDS mapping of as-annealed particles in the image center was also provided (Supporting Information Fig. S2). Fig. 2(b) displays the EDS line scan and the corresponding SEM image of two selected particles highlighted in Fig. 2(a). The EDS line scans confirm that the Au-Ni NPs are homogeneous without any segregation of one metal respecting to the other, though the two metals of Au and Ni are immiscible in the bulk [35]. The uniform mixture of the two elements was confirmed by a quantitative analysis of the EDS point scan of the individual particle, as shown in Fig. 2(c), which approximately agreed with the stoichiometry of the two metals in the bilayer (39 at. % Au and 61 at. % Ni), when the individual Au and Ni layers had the same thickness [34]. The elements of Si, C and O are excluded from the analysis. The TEM and HRTEM images of the as-annealed Au-Ni NPs were taken to obtain the crystallographic information, as shown in Fig. 3. The samples for all the TEM analyses were obtained by sonicating the annealed particles in isopropanol and dropping a small volume on a Cu grid. The HRTEM images in Fig. 3(b) verified the coreshell structure. The lattice spacing of 2.38Å corresponds to the Au (111) planes in the shell and 2.04Å corresponds to Ni (111) planes in the core [15]. **3. Results and discussion** *3.1. Formation of the dual-scale surface structures*

A permanent modification of the surface structure can be made by the laser energy transferred to the silicon surface, leading to the melting and resolidification, vaporization, or ablation of material [30]. The inset of Fig. 1(a) shows the LID in our three-beam laser interference region, and the intensity appears sinusoidal of each interference laser spot. The maximum intensity is calculated to be up to six times of each laser beam, while the minimum value is zero [36]. When the silicon surface was irradiated by the interfered laser beams, the interference field could have different modification effects, which led to the periodic structures with different roughness values. The comparison between the as-ablated silicon surface and the LID is shown in Fig. 4(a). In the high laser intensity region, the silicon was molten, evaporated and resolidified, while in the region of low intensity, the silicon was deposited with a layer of molten silicon and silicon oxide particles due to their expansion from the high intensity area into the background. The feature size of particles was about 10–100nm [37], as shown in Fig. 4(b). The EDS mapping image of as-ablated silicon surface was provided (Supporting Information Fig. S3). The NPs spread around the entire silicon surface within the in terference area, but it would be ablated by the subsequent laser pulses in the high intensity region, which led to the smooth surface in the rim of the hexagon. However, the irradiated area with the LID maxima was formed with the bumps but not the concaves. This phenomenon was explained as the Marangoni effect [38], and it was happened especially when the threshold fluence was used. The height of the bump structure did not increase with the laser fluence. It turned to be flat and finally concaves with the increase of laser fluence. Meanwhile, the process of ablation resulted in the particle melt and clusters deposited in the center of the low intensity region, as shown in Fig. 4(c) and (d). Thus, the laser interference fluences from 300mJ/cm2 to 480mJ/cm2, and laser pulse number of 30 were used in this work. The feature size of the deposited silicon particles can be changed by controlling the laser fluence in the DLIA method, which is discussed in the following section.

3.2. Relationship between the dual-scale structure and the laser fluence The SEM images of the DLIA treated silicon surface evolving with the increasing laser fluence, in the region of 10×10μm2, are shown in Fig. 5(a–e). The bare silicon substrate of (a) was ablated with the laser fluences of 300mJ/cm2 for (b), 360mJ/cm2 for (c), 420mJ/cm2 for (d) and 480mJ/cm2 for (e), respectively. To evaluate the effects of the laser fluence, AFM topographical images of the top surfaces from Fig. 5(a–e) with the resolution of 256×256 pixels were acquired, as shown in Fig. 5(f–j), correspondingly. The height profiles (H) along the white lines in the AFM images of Fig. 5(g–j) were recorded, as shown in Fig. 6(a). The height values have contributions from both the micropattern and the nanostructure. The feature heights of micropatterns were far above the film thickness of 20nm. Nanostructures inside the micropatterned silicon templates led to the formation of the metal NPs. In order to determine the roughness values during the dewetting process, we calculated the root mean square (RMS) roughness Rq of the nanostructures by the corresponding AFM height images according to in the JPK software. The value of Rq for each sample was calculated by averaging the values obtained by three 1×1μm2 central regions of AFM images in Fig. 5(g–j). The statistical errors were also extracted, as shown in Fig. 6(b). Thus, the thickness of the deposited bilayer was above the range of the nanoscale roughness from all samples. The overall height of the microstructure and the roughness of the nanostructure increased with the laser fluence, although the shape of the nanostructure was irregular. As discussed above, the formation of the periodic dual-scale structures wasr esulted from the laser ablation and silicon oxide deposition. The crystallized and highly faceted silicon surface was observed in the case of higher laser fluence. In order to take into account of all scale contributions for the height of structures H and the roughness Rq, no filtering was applied during the calculation [39]. The SEM micrographs of the as-annealed Au-Ni NPs on the template silicon surfaces from Fig. 5(a–e) are shown in Fig. 5(k–o), correspondingly. Upon the annealing procedure,

supersaturated Au-Ni solid-solutions were formed. The NPs obtained on a planar substrate were dispersed irregularly with a broad particle size distribution. The Au-Ni bilayer was assumed as one single component layer without chemical interaction during dewetting. The critical thickness dc, related to the feature size of the substrate topography (structure height and spacing) is identified as an important factor to influence the dewetting process. Instead, the dewetting of the film is not disturbed by the topographic features of the substrate [25,40]. Based on the roughness calculation of the substrates, the thickness of 20nm, in the range of dc, was chosen for the bilayer deposition. Before that, we have tried the thickness of 5nm, 10nm and 30nm on the substrates. It was too thin to be influenced by the nano structures on the substrates for the thickness below 10nm, while the particles formed were too large for the thickness of 30nm. Fig. 7(a) schematically illustrates the effects of the micro/nano structures on the dewetting process of the thin film. On the convex regions of the templates, the film was too thin to be influenced by the micro-topography of the substrates, so that the film did not interact with the microstructures [40]. Therefore, the particles formed on the convex regions were basically the same size as on the bare silicon. On the nanostructures in the concave regions of the templates, the gravity effect was small, and the bilayer was deposited on the top of the nanostructures, leading to the air holes formed under the bilayer and the nanoscale fluctuation on the bilayer (Supporting Information Fig. S4). There were two coexisting mechanisms of nucleation of holes and spinodal dewetting in the dewetting process of bilayer [41]. The holes were the key elements as other defects (inhomogeneities) of edges, impurities and grain boundaries for the initiation of dewetting [42]. Thin metal films were initiated to dewet through the nucleation of holes on them, followed by retracting edges through the capillary-driven surface diffusion, and led to the formation of isolated particles resulting from the Rayleigh instability of the edge retraction [2,43,44]. The particle radius r can be expressed as $r \propto$, where L is the spacing between holes, and d is the film thickness [45]. The higher roughness can leads to more holes under the thin film, and smaller particle radius r. This mechanism also can be explained by the modified spinodal or Rayleigh instability theory, which results in the droplets with a characteristic length scale related to the substrate roughness. It is known that the nano-roughened surface induces a nanoscale fluctuation in the film thickness. The modulation in the film thickness generates pressure on the surface, which drives the liquid metal rivulet breakup into droplets. Thus, the breakup is dependent on the surface tension γ caused by the small amplitudes of film thickness [46]. The length scale $\lambda c=\nu 2\rho/\gamma$, where ν is the kinematic viscosity and ρ the density of the droplet [47]. Higher roughness increases the fluctuation amplitude as well as the surface tension. Thus, the longitudinal pressure gradients are formed. The roughness length scale dominates the capillary length scale and leads to the formation of precise spacing λc and particle size r, as shown in Fig. 7(a). Also, the liquid droplets are not trapped in the valleys between the nanostructures, but on the top of them because of the dewetibility of the nano-roughened surface. According to the Wenzel model of the dewetting of the roughness surface, $\cos\theta=R\cos\theta 0$, where R is a roughness factor of the solid-liquid interface relative to the flat plane, $\theta 0$ is the Young contact angle (CA) of a flat plane and θ is the CA for the droplet on the roughened surface. When $R>1$, the CA with a rough surface is greater than that with a flat surface. Thus, the dewettability property is enhanced by the nano structures on the surface [31]. *3.4. Roughen dependent size distribution of Au-Ni NPs* The metal NPs formed within a $3\times3\mu m2$ region from the center of the nanostructures corresponding to Fig. 5(l—o) (Supporting Information in Fig. S5(a–d)) were used for the calculation of the size distribution of the particles formed on substrates with different roughness values. The results were summarized and plotted by Software Image J and software Origin, as shown in Fig. 8. The difference between the size distributions of the NPs dewetted on the surfaces with different roughness values is evident. Smaller NPs with a narrower size distribution were obtained on

rougher substrates, whereas larger, more irregular NPs were formed on less rougher surfaces. There is only one unique peak value for the roughest substrate of sample O.

3.5. The magnetic properties of the micropatterned NPs

Magnetization curves of the as as-annealed particles in an area of 10cm2 corresponding to Fig. 5(m) were obtained by SQUID at 300K. The coercivity value of 200Oe evidently indicates that the particles are not single-domain after annealing at 950°C. However, the magnetization at about ±2000Oe shows a reversal from a positive magnetization to a diamagnetic state (Supporting Information Fig. S6). In our case, the interfacial effect in the core-shell NPs does not enhance the positive magnetization but causes negative magnetization. It is probably due to the diamagnetic contribution from the Au shell [48]. There seems to be an optimum thickness of the Au shell which will show the maximum magnetization, beyond which the diamagnetism will dominate. The AFM topological image and the MFM image at the magnetic remanence for the Au-Ni particles were obtained to further characterize the NP patterns. Fig. 10, including 7 hexagonal cells in Fig. 5(m), shows the AFM and MFM comparison images of the 20×20μm2 NP patterned surfaces. The topography was recorded in the tapping mode in the first scan, and then the lock-in phase was recorded with a lifted probe height of 300nm to ensure the magnetic force map was independent of the NP topography [49]. The magnetic domain pattern in Fig. 10(b) is in agreement with the topographical pattern in Fig. 10(a). The images also clarify the uniformity of the Ni material in the NP patterns. The height of the particles was measured to be 322nm, corresponding to the maximum particle size on the nanostructured substrate, as shown in Fig. 8. However, there is no significant magnetic contrast (dark and light sections), but a complex magnetic domain structure in the MFM image. The vortices (black circles) visible in the middle of NPs confirm the hysteresis loop shape in Fig. 9. The particles exhibit weak magnetic crystallographic anisotropy probably because of the high crystallinity formed during the annealing. The NPs in the samples were with a diameter of over 100nm, which exceeds the critical dimension for the single-domain state, and there is a high probability of vortex structures beingformed [50]. Ordered magnetic structures with oriented directions can be obtained by realigning the vortex structure through an external magnetic field [51] (Supporting Information Fig. S7). Furthermore, the AFM and MFM comparison images of the 10×10μm2 NP patterned surfaces including one hexagonal cell in Fig. 5(n) was obtained (Supporting Information Fig. S8). The probe was lifted over the height of 300nm from the NP topography. The measured height of the particles was 275nm, which was in agreement with the maximum particle size in Fig. 8.

4. Conclusion

In summary, this study has demonstrated that patterned bimetal NP arrays can be successfully fabricated on the dual-scale-structured silicon substrates by the templated dewetting method. The microscale topography in conjunction with the nanoscale structures obtained at the same time by the DLIA method created dual-scale surface structures, which were used as the templates for the self-assembly of patterned NPs. In addition to the NP pattern formation based on the templates, the dewetting on nanostructured surfaces enabled a significant reduction in the particle size and more uniform distribution due to the modified Rayleigh instability. Meanwhile, the magnetic domain pattern of as-annealed Au-Ni NPs is in agreement with the topographical pattern of the NPs as well as the silicon template. With the employed mask and chemical-free method, Au-Ni NPs and other bimetal combinations can be produced with controllable micro-patterns and NP sizes for the applications such as catalysis, data storage and other functional nanostructured elements and devices.

Declaration of Competing Interest

The authors declare that they have no known competing financial interests or personal relationships that could have appeared to influence the work reported in this paper.

Acknowledgments
This work was supported by National Key R&D Program of China (No. 2016YFE0112100), EU H2020 Program (FabSurfWAR No.644971; NanoStencil No.767285), National Natural Science Foundation Program of China (No.11504030, No.61964007), Jilin Provincial Science and Technology Program (Nos.20160623002TC, 20180414002GH, 20180414081GH, 20180520203JH and 20190702002GH), and "111" Project of China (D17017).

Appendix A. Supplementary data
Low magnification SEM image of NP arrays, higher magnification EDS mapping of dewetted particles, EDS mapping image of the as-ablated silicon surface, SEM image of the as-deposited silicon surface with bilayer metal film, magnified SEM images of the as-annealed Au-Ni NPs, magnetization curves of as-annealed patterned surface, MFM images at reversed magnetic fields and MFM images of the as-annealed patterned surface (TIFF). Supplementary data to this article can be found online at https://doi.org/10.1016/j.jmmm.2019.165876.

References
[1] V.V. Temnov, G. Armelles, U. Woggon, D. Guzatov, A. Cebollada, A. Garcia-Martin, J.M. Garcia-Martin, T. Thomay, A. Leitenstorfer, R. Bratschitsch, Active magneto-plasmonics in hybrid metal–ferromagnet structures, Nat. Photonics 4 (2010) 107.
[2] Y.A. Akimov, K. Ostrikov, E.P. Li, Surface plasmon enhancement of optical absorption in thin-film silicon solar cells, Plasmonics 4 (2009) 107–113.
[3] S. Yang, F. Xu, S. Ostendorp, G. Wilde, H. Zhao, Y. Lei, Template-confined dewetting process to surface nanopatterns: fabrication, structural tunability, and structure-related properties, Adv. Funct. Mater. 21 (2011) 2446–2455.
[4] S. Hong, T. Kang, D. Choi, Y. Choi, L.P. Lee, Self-assembled three-dimensional nanocrown array, ACS Nano 6 (2012) 5803.
[5] L. Zhou, C. Zhang, M.J. Mcclain, A. Manjavacas, C.M. Krauter, S. Tian, F. Berg, H.O. Everitt, E.A. Carter, P. Nordlander, Aluminum nanocrystals as a plasmonic photocatalyst for hydrogen dissociation, Nano Lett. 16 (2016) 1478–1484.
[6] J.E. Yoo, K. Lee, M. Altomare, P.E. Selli, P.P. Schmuki, Self-organized arrays of single-metal catalyst particles in TiO2 cavities: a highly efficient photocatalytic system, Angew. Chem. 52 (2013) 7514–7517.
[7] D. Wang, Y. Li, Bimetallic nanocrystals: liquid-phase synthesis and catalytic applications, Adv. Mater. 23 (2011) 1044.
[8] H.A. Elsayed, H.M. Molero, V.I. Birss, The impact of fabrication conditions on the quality of Au nanoparticle arrays on dimpled Ta templates, Nanotechnology 23 (2012) 435602.
[9] S.J. Lister, T. Thomson, J. Kohlbrecher, K. Takano, V. Venkataramana, S.J. Ray, M.P. Wismayer, M.A.D. Vries, H. Do, Y. Ikeda, Size-dependent reversal of grains in perpendicular magnetic recording media measured by small-angle polarized neutron scattering, Appl. Phys. Lett. 97 (2010) 011301.
[10] O. Hellwig, A. Berger, T. Thomson, E. Dobisz, Z.Z. Bandic, H. Yang, D.S. Kercher, E.E. Fullerton, Separating dipolar broadening from the intrinsic switching field distribution in perpendicular patterned media, Appl. Phys. Lett. 90 (2007) R199.
[11] J. Lisa, K. Daniel, K. Rahel, R. Johannes, T. Piriya, W. Anja, R. Lutz, W.M. Christopher, Recent developments of magnetoresistive sensors for industrial applications, Sensors 15 (2015) 28665–28689.
[12] M.C. Mcalpine, H. Ahmad, D. Wang, J.R. Heath, Highly ordered nanowire arrays on plastic substrates for ultrasensitive flexible chemical sensors, Nat. Mater. 6 (2007) 379–384.

[13] M. Sakamoto, T. Tachikawa, M. Fujitsuka, T. Majima, Photochemical formation of Au/Cu bimetallic nanoparticles with different shapes and sizes in a poly(vinyl alcohol) film, Adv. Funct. Mater. 17 (2010) 857–862.
[14] K. Wong, Y. Zhou, M. Wu, Y. Lei, Ni/Au hybrid nanoparticle arrays as a highly efficient, cost-effective and stable SERS substrate, RSC Adv. 5 (2014) 6172–6180.
[15] H. She, Y. Chen, X. Chen, K. Zhang, D.L. Peng, Structure, optical and magnetic properties of Ni@Au and Au@Ni nanoparticles synthesized via non-aqueous approaches, J. Mater. Chem. 22 (2012) 2757–2765.
[16] R. Hughes, E. Menumerov, S. Neretina, When lithography meets self-assembly: a review of recent advances in the directed assembly of complex metal nanostructures on planar and textured surfaces, Nanotechnology 28 (2017) 282002.
[17] B. Elena, D. Neus, O.J. Isaac, R.M. Daniel, Structuration and integration of magnetic nanoparticles on surfaces and devices, Small 8 (2012) 1465–1491.
[18] D. Nepal, M.S. Onses, K. Park, M. Jespersen, C.J. Thode, P.F. Nealey, R.A. Vaia, Control over position, orientation, and spacing of arrays of gold nanorods using chemically nanopatterned surfaces and tailored particle-particle-surface interactions, ACS Nano 6 (2012) 5693–5701.
[19] L. Wang, L. Dong, L. Li, Z. Weng, H. Xu, M. Yu, Z. Wang, Fabrication of periodically micropatterned magnetite nanoparticles by laser-interference-controlled electrodeposition, J. Mater. Sci. 53 (2018) 3239–3249.
[20] M. Altomare, N.T. Nguyen, P. Schmuki, Templated dewetting: designing entirely self-organized platforms for photocatalysis, Chem. Sci. 7 (2016) 6865–6886.
[21] Y.J. Oh, J.H. Kim, C.V. Thompson, C.A. Ross, Templated assembly of Co-Pt nanoparticles via thermal and laser-induced dewetting of bilayer metal films, Nanoscale 5 (2012) 401–407.

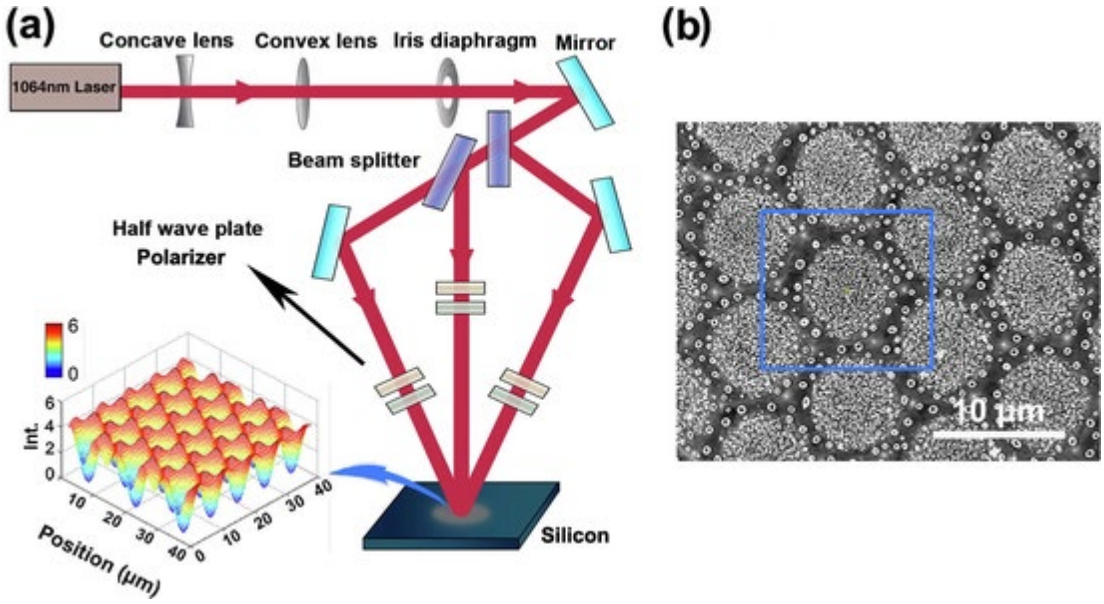

Fig. 1. (a) Diagram of three-beam laser interference ablation setup. The inset is the simulated laser intensity distribution of DLIA (λ=1064nm, θ=4.1°). (b) SEM image of dewetted Au-Ni NP arrays. The silicon samples were treated with the interference fluence of 420mJ/cm2.

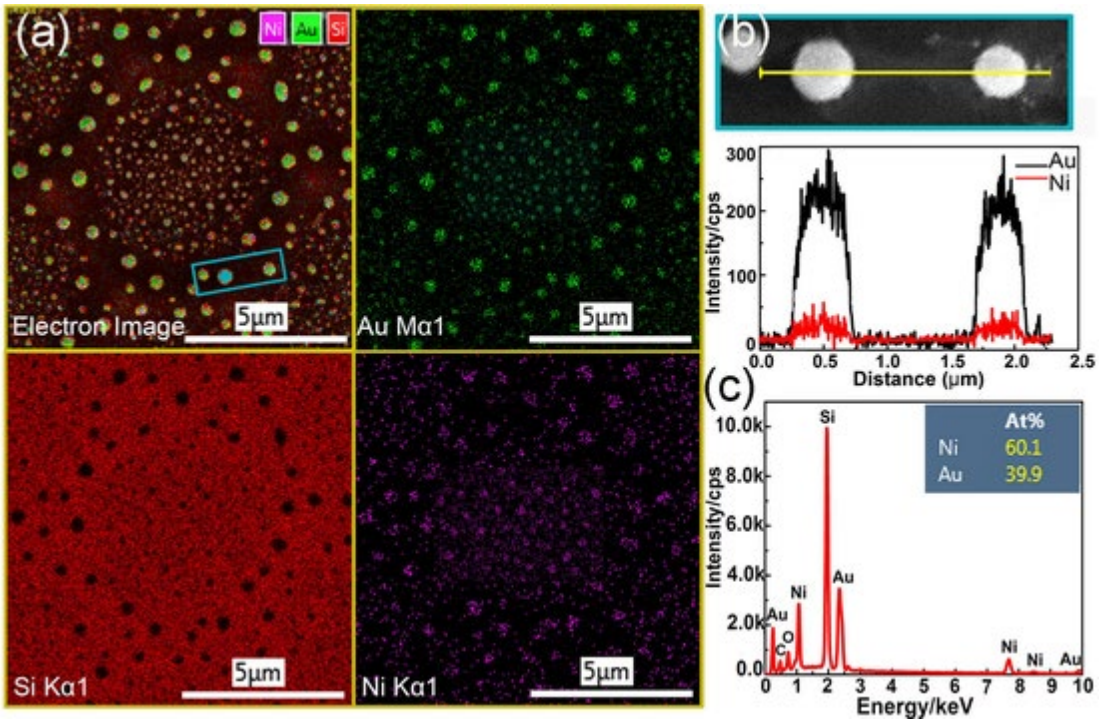

Fig. 2. (a) EDS mapping image of the as-annealed Au-Ni particles on the silicon substrate. Yellow part is the overlap of the Au (green), Si (red), and Ni (pink) EDS maps. (b) The EDS line scans two Au-Ni particles highlighted with the blue square in (a), and the yellow line illustrates the EDS line scan performed. (c) The EDS spectrum of the particle highlighted with the blue cross in (a). (For interpretation of the references to colour in this figure legend, the reader is referred to the web version of this article.)

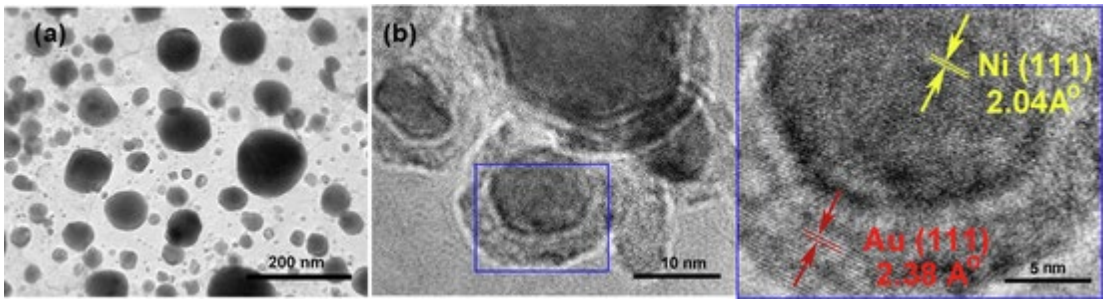

Fig. 3. (a) TEM image of the as-annealed Au-Ni nanoparticles. (b) HRTEM image of a single NP showing the lattice fringes belonging to the core and shell component.

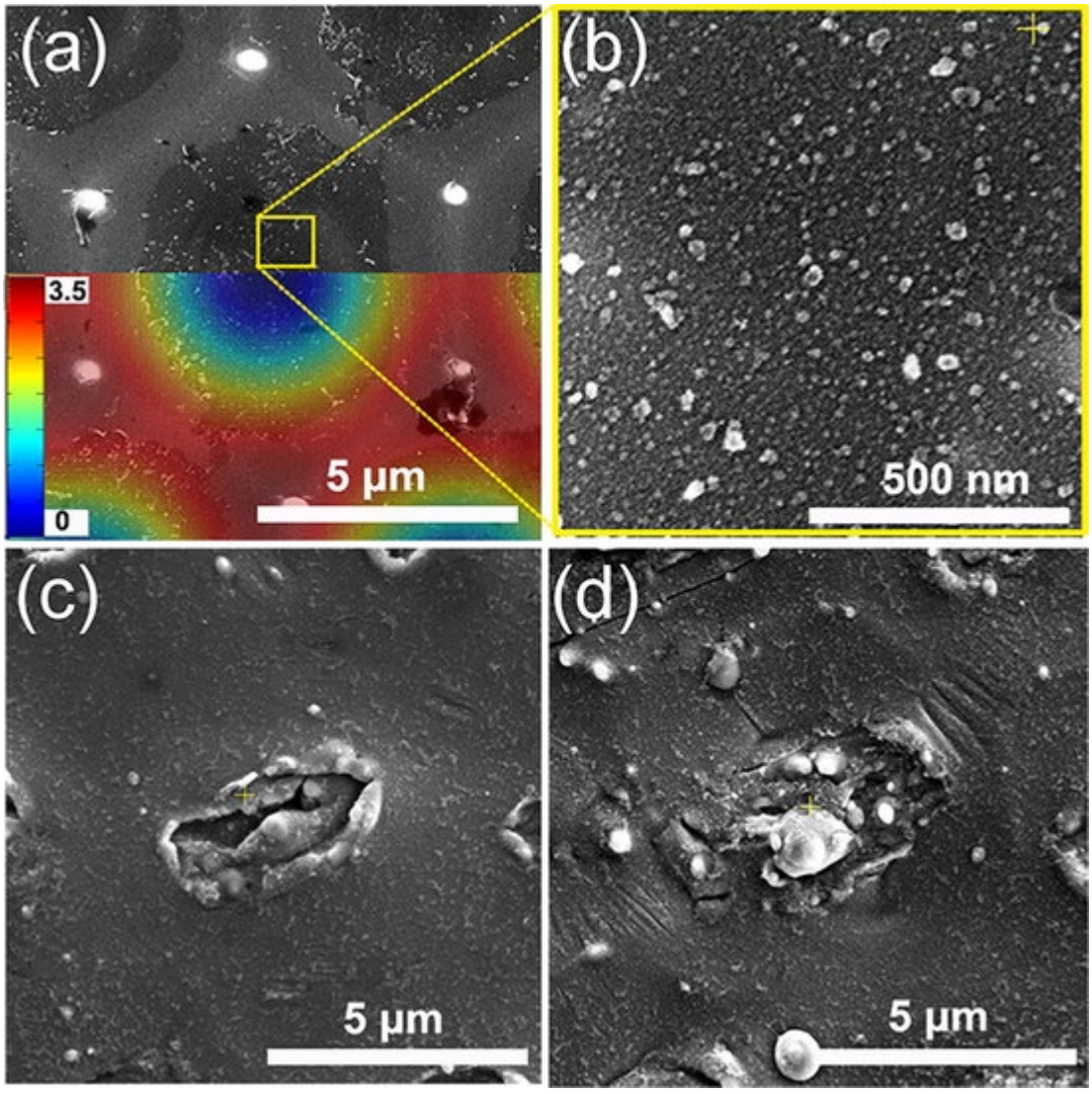

Fig. 4. SEM images of one DLIA treated hexagonal cell silicon surface with different laser parameters. (a) The interference fluence of 420mJ/cm2 near the melting threshold. (b) The high magnification SEM image of the nanostructures in the yellow inset of (a). (c,d) The interference fluences of 540mJ/cm2 and 600mJ/cm2, respectively. Laser pulse number of 30 was used for all the samples.

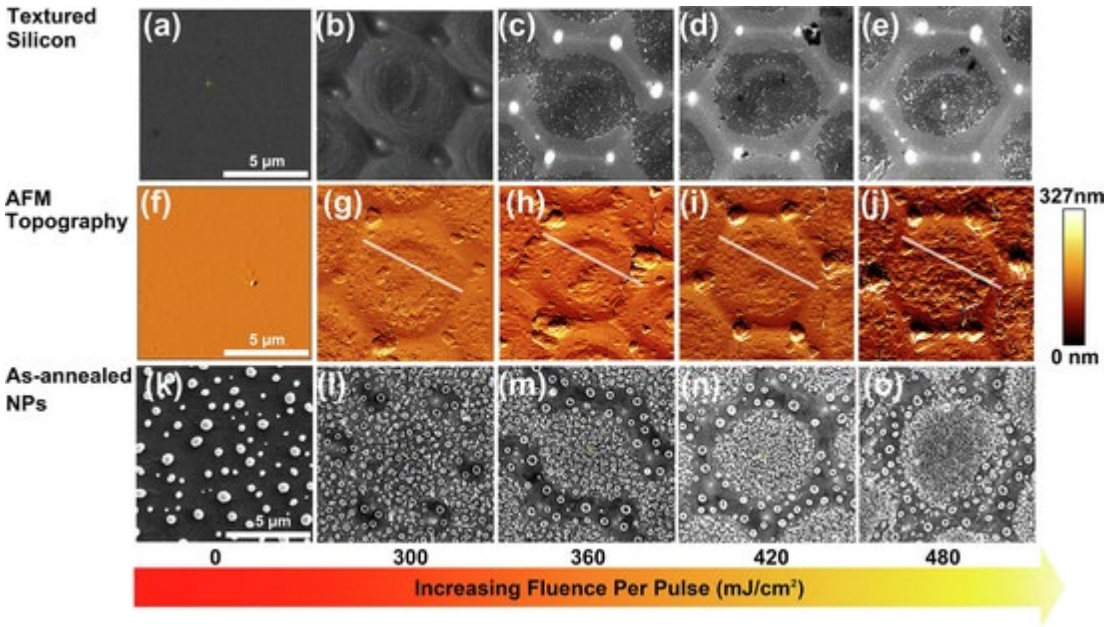

Fig. 5. (a–e) SEM images of representative individual hexagonal cells of the as-ablated silicon evolving with the increasing fluence. (f–j) AFM topography images corresponding to (a–e), and (k–o) SEM images of the as-annealed Au-Ni NPs on the silicon templates corresponding to (a–e). The treating laser fluences were 300mJ/cm2 for (b, g, l), 360mJ/cm2 for (c, h, m), 420mJ/cm2 for (d, i, n) and 480mJ/cm2 for (e, j, o), respectively and 30 pulses were used for all the samples. (a) SEM micrograph of bare silicon substrate before deposition.

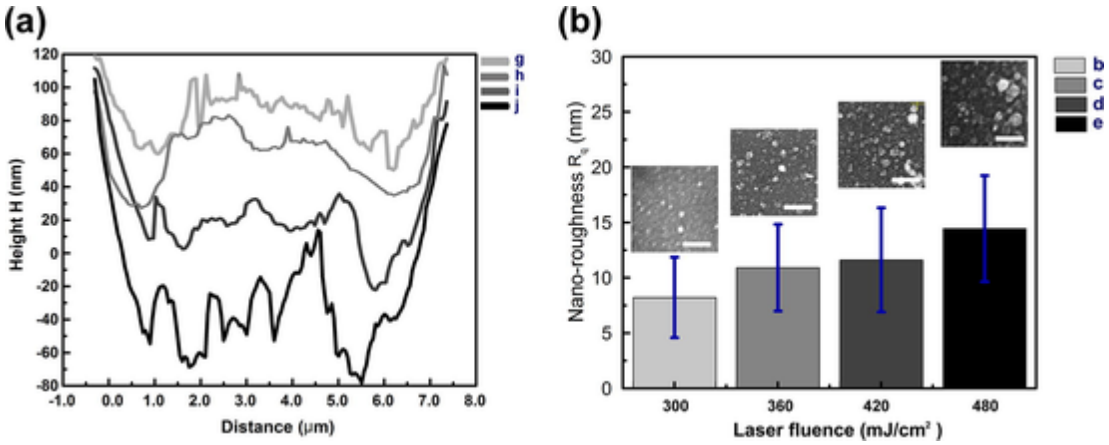

Fig. 6. (a) AFM height profiles (H) along the indicated white lines corresponding to Fig. 5(g–j). (b) The RMS roughness Rq of the nanostructure top surface within the central area of 1×1μm2 corresponding to Fig. 5(b–e), analyzed by AFM software (scale bar: 200nm).

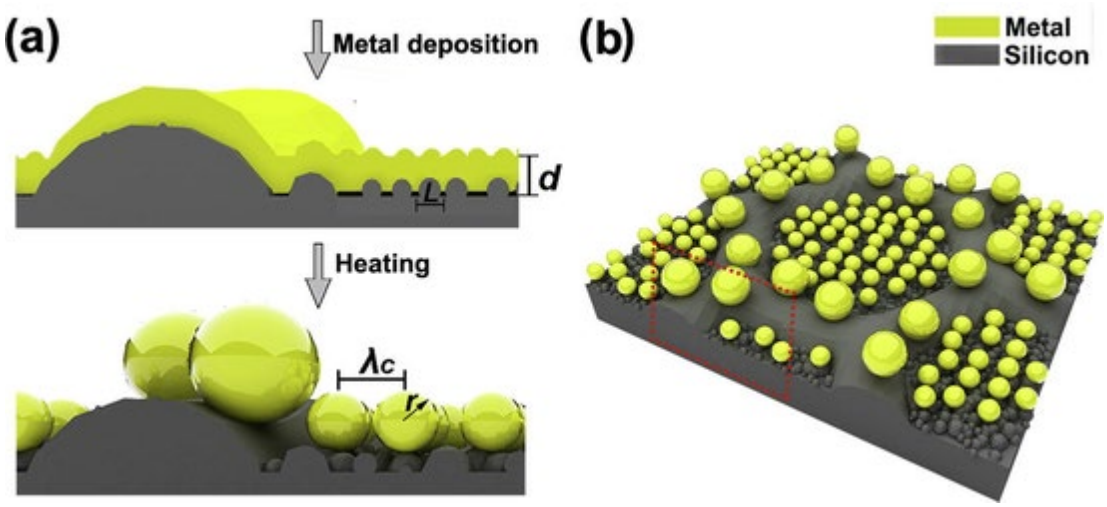

Fig. 7. (a) Mechanism of the templated dewetting of metal bilayer on the micro/nano dual-scale surface structures. (b) Sketch of one hexagonal cell of the dewetted Au-Ni NP arrays. The side view of the red area in (b) is shown in (a).

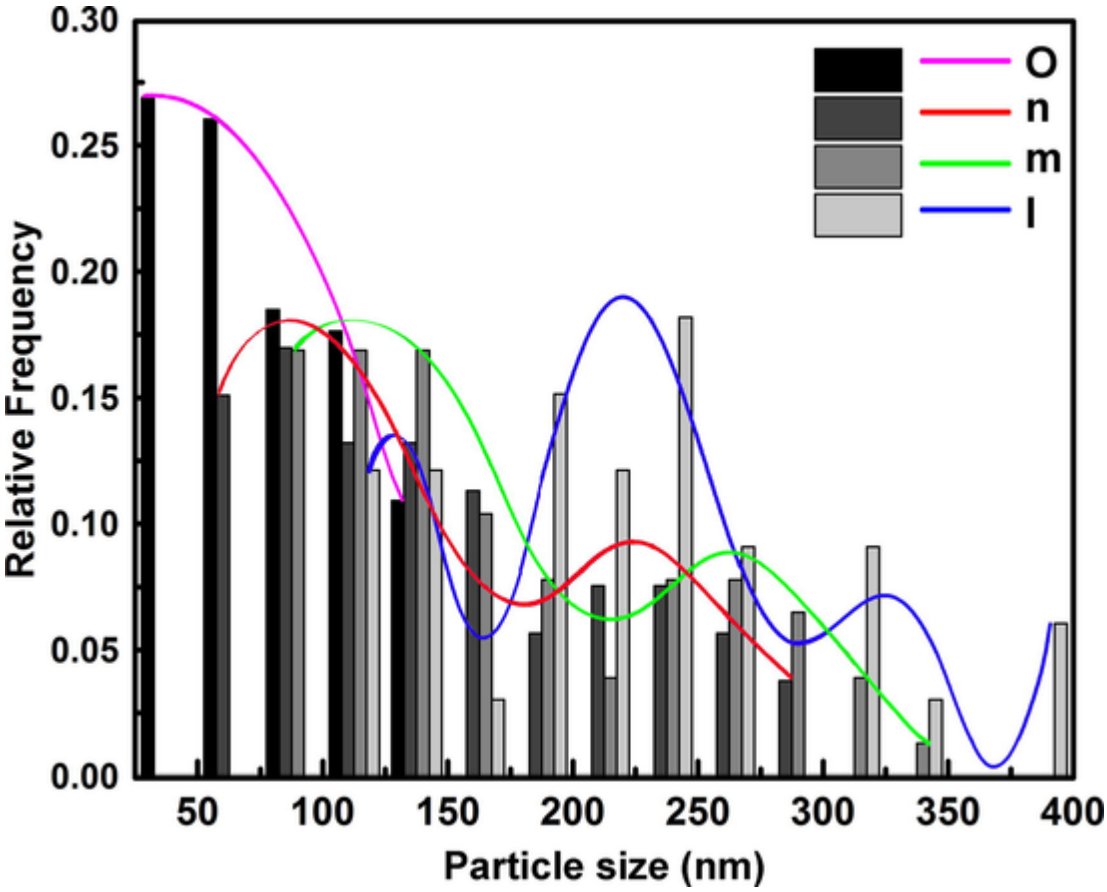

Fig. 8. Plots of the size distributions of the dewetted Au-Ni particles in the central area of 3×3μm2 corresponding to Fig. 5(l–o).

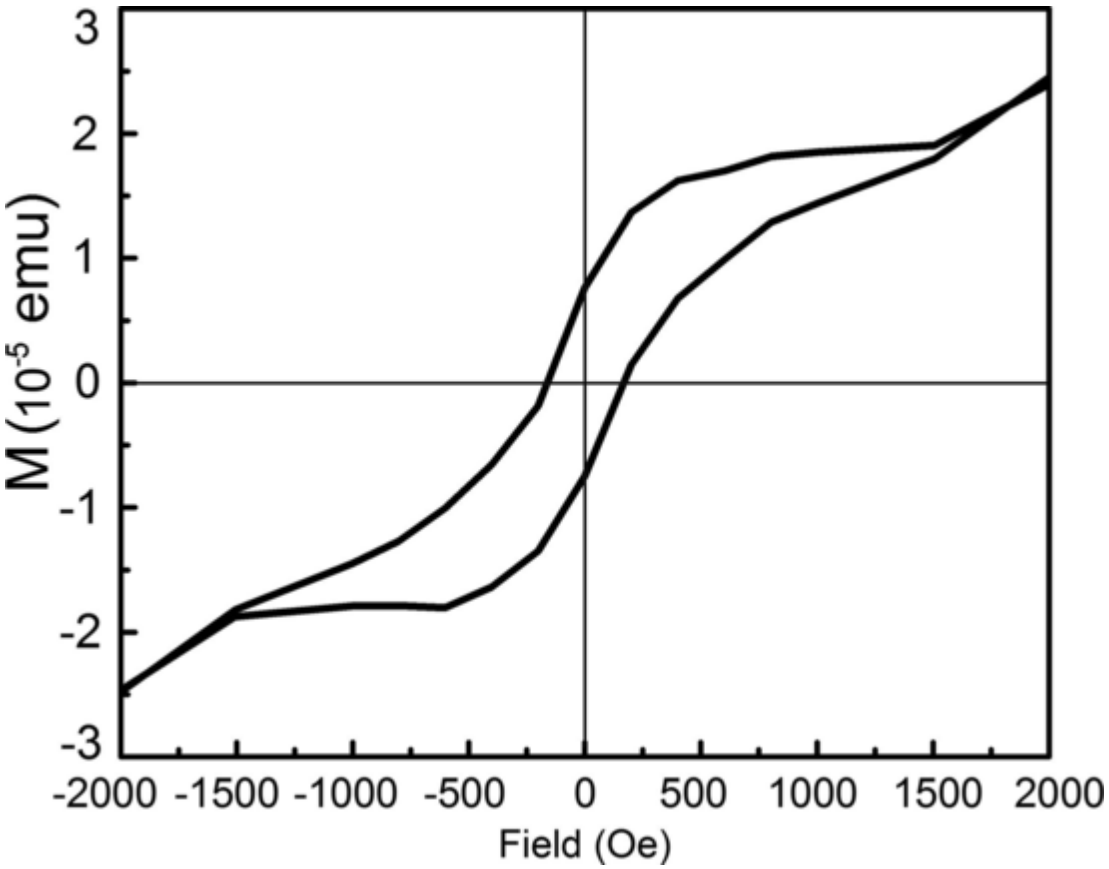

Fig. 9. Room-temperature magnetization curves of as-annealed patterned surface within the area of 10cm2 corresponding to Fig. 5(m)

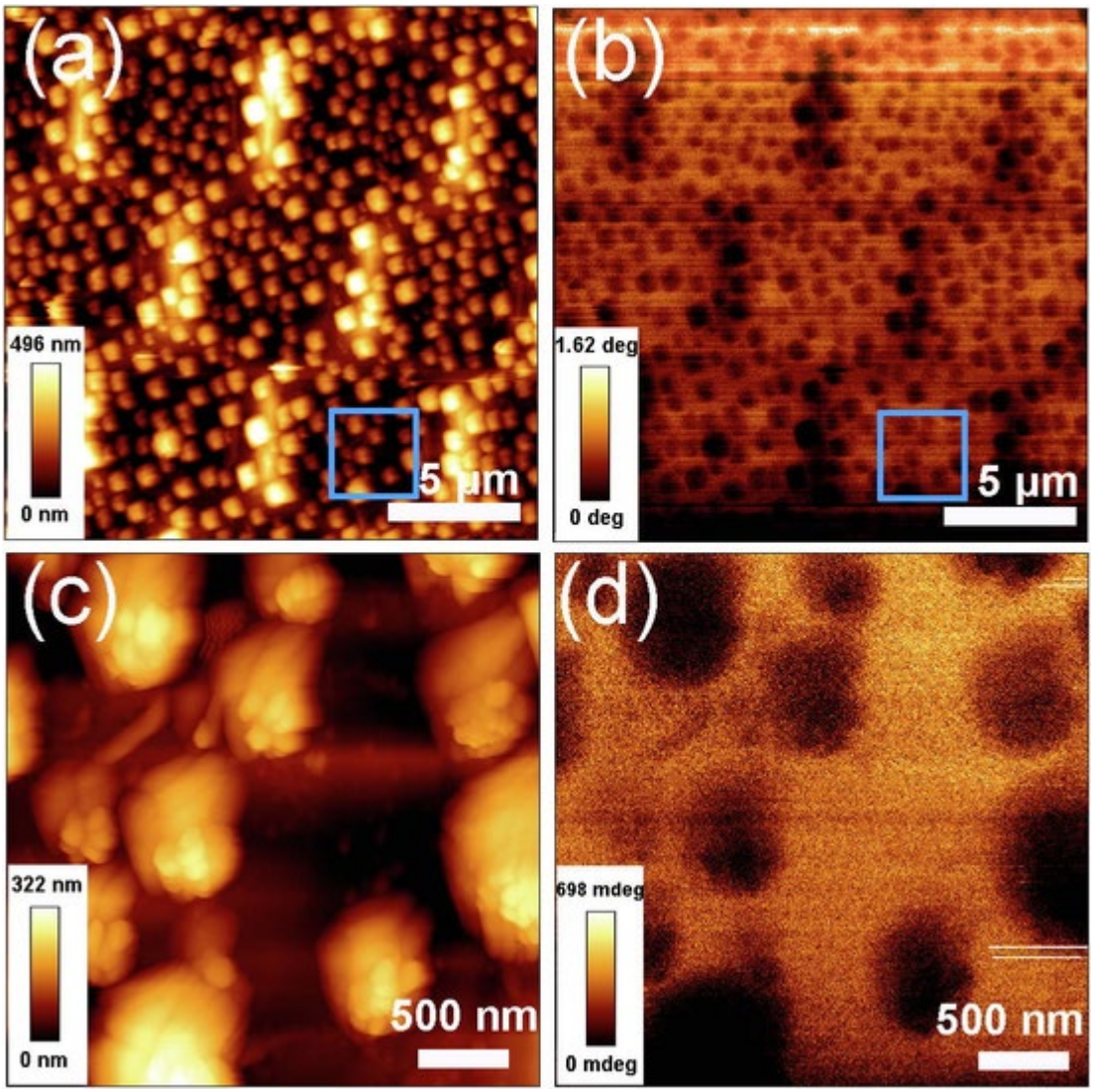

Fig. 10. MFM images of the as-annealed patterned surface within the area of 20×20µm2 corresponding to Fig. 5(m). AFM topographical images of (a) and (c), and the corresponding MFM images of (b) and (d). Blue areas of 3×3µm2 in (a) and (b) highlight the locations scanned for (c) and (d), respectively.